

Article

Radiometric Cross-Calibration of Tiangong-2 MWI Visible/NIR Channels over Aquatic Environments using MODIS

Qu Zhou ¹ , Liqiao Tian ¹, Jian Li ^{2,*}, Qingjun Song ^{3,4} and Wenkai Li ¹

¹ State Key Laboratory of Information Engineering in Surveying, Mapping and Remote Sensing, Wuhan University, Wuhan 430079, China; quzhou@whu.edu.cn (Q.Z.); tianliqiao@whu.edu.cn (L.T.); lwk1542@hotmail.com (W.L.)

² School of Remote Sensing and Information Engineering, Wuhan University, Wuhan 430079, China

³ National Satellite Ocean Application Service, State Oceanic Administration, Beijing 10089, China; kingdream@mail.nsoas.org.cn

⁴ Key Laboratory of Space Ocean Remote Sensing and Application, State Oceanic Administration, Beijing 10089, China

* Correspondence: lijian@whu.edu.cn; Tel.: +86-027-68778229

Received: 7 September 2018; Accepted: 12 November 2018; Published: 14 November 2018



Abstract: The Moderate-Resolution Wide-Wavelength Imager (MWI), onboard the Tiangong-2 (TG-2) Space Lab, is an experimental satellite sensor designed for the next-generation Chinese ocean color satellites. The MWI imagery is not sufficiently radiometrically calibrated, and therefore, the cross-calibration is urgently needed to provide high quality ocean color products for MWI observations. We proposed a simple and effective cross-calibration scheme for MWI data using well calibrated Moderate Resolution Imaging Spectroradiometer (MODIS) imagery over aquatic environments. The path radiance of the MWI was estimated using the quasi-synchronized MODIS images as well as the MODIS Rayleigh and aerosol look up tables (LUTs) from SeaWiFS Data Analysis System 7.4 (SeaDAS 7.4). The results showed that the coefficients of determination (R^2) of the calibration coefficients were larger than 0.97, with sufficient matched areas to perform cross-calibration for MWI. Compared with the simulated Top of Atmosphere (TOA) radiance using synchronized MODIS images, all errors calculated with the calibration coefficients retrieved in this paper were less than 5.2%, and lower than the lab calibrated coefficients. The Rayleigh-corrected reflectance (ρ_{rc}), remote sensing reflectance (R_{rs}) and total suspended matter (TSM) products of MWI, MODIS and the Geostationary Ocean Color Imager (GOCI) images for Taihu Lake in China were compared. The distribution of ρ_{rc} of MWI, MODIS and GOCI agreed well, except for band 667 nm of MODIS, which might have been saturated in relatively turbid waters. Besides, the R_{rs} used to retrieve TSM among MWI, MODIS and GOCI was also consistent. The root mean square errors (RMSE), mean biases (MB) and mean ratios (MR) between MWI R_{rs} and MODIS R_{rs} (or GOCI R_{rs}) were less than 0.20 sr^{-1} , 5.52% and within 1 ± 0.023 , respectively. In addition, the derived TSM from MWI and GOCI also agreed with a R^2 of 0.90, MB of 13.75%, MR of 0.97 and RMSE of 9.43 mg/L. Cross-calibration coefficients retrieved in this paper will contribute to quantitative applications of MWI. This method can be extended easily to other similar ocean color satellite missions.

Keywords: atmospheric correction; cross calibration; open oceans; total suspended matter; inland water

1. Introduction

The newest-generation Chinese ocean color experimental sensor, the Moderate-Resolution Wide-Wavelengths Imager (MWI), onboard the Tiangong-2 (TG-2) space lab was launched on 15 September 2016. The MWI will enable China to load ocean-color satellite sensors onboard ocean series satellites in the future and provides more satellite data for aquatic remote sensing of the Earth [1]. The MWI uses a push-broom imaging system similar to the Medium Resolution Imaging Spectrometer (MERIS) onboard the ENVISAT satellite and the Ocean and Land Color Instrument (OLCI) onboard the Sentinel-3A satellite. It has a 100 m spatial resolution and 14 bands in the visible and near-infrared spectrum, two shortwave infrared bands and two thermal infrared bands [2]. The MWI consists of three imaging modules: A visible light and near-infrared wavelength module (VIS/NIR, 100 m) for ocean color observations, a shortwave infrared wavelength module (SWIR, 200 m) for atmospheric correction (AC) in turbid waters, and a thermal infrared module (TIR, 400 m) for measuring the sea surface temperature. In addition, MWI has a general field of view (FOV) angle of 42° and a swath width of 300 km [3].

MWI will supplement ocean color remote sensing, which has played a significant role in monitoring oceanic and freshwater ecosystems [4]. MWI has many visible and NIR bands, as well as a higher spatial resolution (100 m) than those of current mainstream ocean-color sensors [1]. During the past three decades, more than 20 satellite ocean color sensors were launched, such as the Sea-viewing Wide Field-of-View Sensor (SeaWiFS), the Moderate Resolution Imaging Spectroradiometer (MODIS), the Communication, Ocean, and Meteorological Satellite (CMOS)/Geostationary Ocean Color Imager (GOCI) and the recent Sentinel series. The first generation Chinese ocean color satellites are known as HY-1A, HY-1B [5], and the HY-1C/HY-1D. MWI is a new on-orbit Chinese ocean color sensor at the highest spatial resolution. Satellite sensors at a moderate spatial resolution offer an unparalleled opportunity to observe global and regional dynamics of land surfaces, the atmosphere and water resources [6]. Therefore, the MWI may provide a new opportunity to obtain high quality spectral data for remote sensing applications over oceanic and inland waters, especially for those with severe eutrophication, highly turbid waters, and small lakes and reservoirs.

The qualitative uses for the TG-2/MWI images, however, require accurate radiometric calibration. The most commonly used on-orbit calibration techniques are vicarious calibration and cross-calibration [7–11]. In general, vicarious calibrations are challenging because of their labor intensity, high cost, small dynamic range, and limited spatial coverage among other factors [12]. Furthermore, this approach cannot be used to calibrate historical sensor data [13]. To overcome these limitations, cross-calibration approaches have been developed that use a well-calibrated satellite sensor as a reference. Cross-calibration can provide a calibrating accuracy as high as that of the vicarious calibration technique, at much lower cost and at a higher frequency [14]. This approach has been successfully used in a number of remote-sensing instruments [15,16]. Thus, cross-calibration is an alternative way to radiometrically calibrate the TG-2/MWI images at a high accuracy and low cost.

Many cross-calibration experiments have been conducted at land-based calibration sites such as the Dunhuang calibration site in China, rather than in aquatic environments. Previous studies calibrated a target sensor using Landsat sensors as the reference [14,17,18]. Those studies assumed that the Top of Atmosphere (TOA) radiance or reflectance of the two sensors are equal. Several Chinese high-resolution sensors [19] have been successfully cross-calibrated with Landsat-8/OLI as a reference sensor, using a spectrum matching cross-calibration method [13], an image-based cross-calibration method [20] or a data assimilation cross-calibration method [14]. The Second Simulation of the Satellite Signal in the Solar Spectrum model (6S) [21] was used for the AC. This method is appropriate when the aerosol model is known and the sensor is designed for land objects. As the MWI is an ocean color remote sensing sensor, it is more interesting to conduct cross-calibration for MWI over aquatic environments. The crucial procedure in cross-calibration requires the simulation of the path radiance or reflectance of the target sensor using a reference sensor.

The path radiance of MWI can be estimated using an AC algorithm, which is the most important part in cross-calibration over aquatic environments, because the signal from the water column is small [22]. The standard AC algorithm (NIR-AC) is relatively stable and reliable for case 1 waters [23]; however, it fails when applied to case 2 waters (the definitions of case 1 and 2 waters were described by Reference [24]). The failure results from the invalid black water assumption at NIR bands [25]. For case 2 waters, the shortwave infrared atmospheric correction (SWIR-AC) is useful with a black water assumption in the shortwave infrared wavelengths [26]. Although the SWIR-AC method shows improved ocean color products in the case 2 waters, its performance in the case 1 ocean waters is usually worse than the NIR-AC method [27], with more noises in the ocean color products. Thus, atmospheric correction should be selected carefully to better calibrate the TG-2/MWI.

For case 1 water, the water and aerosol make only a small contribution to the TOA radiance, while the Rayleigh scattering of gas molecules contributes a large proportion of TOA signal [28]. The NIR-AC algorithm assumes that the signal from the water is negligible in the NIR region, and determines the aerosol properties using two NIR bands [23], because the Rayleigh scattering can be calculated accurately with a uncertainty less than 1% [29]. After the aerosol properties are known, the aerosol contribution at the visual bands could be determined, and then the water signal in visual region can be calculated. Thus, using the open ocean waters as calibration sites could take advantages of the NIR-AC algorithm.

In this study, we proposed a simple and effective cross-calibration method for the newly launched MWI sensor over open ocean waters. The proposed method cross-calibrated MWI images with MODIS data, as MODIS has similar ocean color bands to MWI and provides highly improved radiometric calibration, sensitivity and spectral bands [22]. The surface and atmospheric conditions were assumed to be unchanged during the overpassing time of the target and reference instruments, and the TOA signals of the two sensors were identical when the difference in spectral responses and view geometries were adjusted [12]. For a remote-sensing satellite over water targets, the total TOA signals consist of the Rayleigh scattering signal, aerosol scattering signal and the water-leaving signals (the signals of sun glints and whitecaps are ignored). In our approach, the Rayleigh scattering and aerosol scattering of the MWI were estimated with MODIS images based on the NIR-AC algorithms [23,26,27]. We evaluated the accuracy of the cross-calibration coefficients by comparing the TOA radiance simulated from synchronized MODIS imagery with the TOA radiance from the calibration coefficients. We also compared the Rayleigh-corrected reflectance (ρ_{rc}), remote sensing reflectance (R_{rs}) and total suspended matter (TSM) products in Taihu Lake, derived from the MWI image using the cross-calibrated coefficients with those products from MODIS and GOCI images.

2. Datasets

2.1. Study Area

In general, the calibration sites should be temporally, spatially and radiationally stable in brightness, spatial homogeneity, altimetric and bidirectional effects [30]. Some targets should be located in the calibration site and used as 'dark' objects [31] to determine the aerosol optical depth accurately such as clean lakes. In this paper, the open ocean waters were used as calibration sites for three reasons: (1) Open ocean waters are relatively stable during a short time period; (2) open ocean waters can be considered as 'dark' objects and used to estimate the aerosol optical depths; (3) the atmosphere correction algorithm for "clean" waters is relatively reliable. In our research, six match-ups between MWI and MODIS were collected at open oceans. The locations of the open ocean waters are shown in Figure 1.

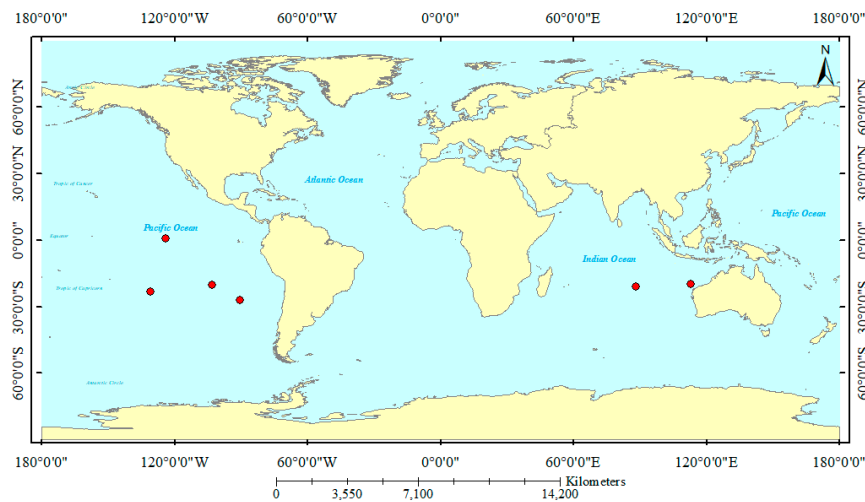


Figure 1. The location of the open ocean waters that were used as calibration sites in this study (red points).

2.2. MODIS and MWI Match-Ups

The MODIS and MWI match-ups play a crucial role in cross-calibration. Since the launch of MODIS (Terra in 1999 and Aqua in 2002; <https://modis.gsfc.nasa.gov/>), the imagery from MODIS has been widely used in ocean color remote sensing, including for the retrieval of ocean color products, sea surface temperature products, and the evaluation of products (<https://oceancolor.gsfc.nasa.gov/>). In addition, MODIS has also been widely used in cross-calibration for other ocean color sensors [9,22,32]. MWI is a new Chinese ocean color sensor that has spectral characteristics similar to those of MODIS, including some enhancements. A comparison of the band settings, spectral range, signal-to-noise ratio (SNR), swath width, and orbit height between TG-2/MWI and MODIS/Aqua is provided in Table 1. The MODIS was selected as the reference sensor for the following reasons: (1) MODIS is widely used in ocean color remote sensing; (2) the MODIS instruments have demonstrated low levels of radiometric calibration errors [12]; (3) the band settings between MWI and MODIS are similar; (4) the temporal resolution of MODIS is high (once a day at low to moderate latitude) making it easy to find match-ups between MWI and MODIS.

The MWI-MODIS match-ups are essential in the proposed cross-calibration method. Several principles should be followed [33]: (1) The MWI and MODIS images for open ocean areas should be cloudless and without sun glints and whitecaps (areas with low wind speed [22]); (2) the time difference between overpasses of MWI and MODIS should be less than three hours; and (3) at least two regions should be selected. All the images should be collected during a short period of time to eliminate radiometric degradation of both instruments [12]. In practice, 1491 MWI images were first collected for cross-calibration during a short period of time between October 2016 and December 2016. Then, visual examinations were conducted to find homogeneous areas and avoid large aerosol changes, cloud contamination, and sun glints within these selected image pairs. In total, six near-simultaneous MWI-MODIS match-ups were finally selected for calibration and five match-ups for validation. The acquisition times and viewing geometries are listed in Table 2. The largest difference between both sun and view zenith angles of MWI and MODIS is 23.98° , and the largest zenith angle is about 51° ($<60^\circ$). When the zenith is $>60^\circ$, the bidirectional effects increase rapidly [34].

Table 1. Comparison between Moderate-resolution Wide-wavelength Imager (MWI)/Tiangong-2 (TG-2) and Moderate Resolution Imaging Spectroradiometer (MODIS)/Aqua bands.

TG-2/MWI				Aqua/MODIS			
Band ^a	Center Wavelength ^b	Spectral Range ^b	SNR ^c	Band	Center Wavelength	Spectral Range ^b	SNR ^d
V1	413	403–423	390	8	413	405–420	880
V2	443	433–453	515	9	443	438–448	838
V3	490	480–500	557	10	488	483–493	802
V4	520	510–530	556	11	531	526–536	754
V5	565	555–575	555	12	551	546–556	750
V7	665	655–675	399	13	667	662–672	910
V8	682.5	677.5–687.5	273	14	678	673–683	1087
V9	750	740–760	302	15	748	743–753	586
V11	865	845–885	255	16	869	862–877	516
Swath Width		300 km		2330 km			
Orbit Height		386 km		705 km			

^a V12 (904 nm), V13 (940 nm) and V14 (980 nm) of MWI were not considered because the wavelengths are longer than MODIS ocean color bands, and V6 (620 nm) and V10 (820 nm) were also not calibrated for lack of matched MODIS bands; ^b Center wavelength and Spectral Range are in nm; ^c TG-2/MWI SNRs are from [2]; ^d MODIS/Aqua SNR are required SNR from (<https://modis.gsfc.nasa.gov/about/specifications.php>).

Table 2. Acquisition Times and imaging angles of MWI and MODIS match-ups (Greenwich Mean Time).

Match-UPs Scenes		Acquisition Time (DD/MM/YYYY HH:MM)	Solar Zenith Angle (°)	Sensor Zenith Angle (°)	Time Difference (minute)
Match-up 1	MWI	14/12/2016 01:25 a.m.	39.08	22.05	70
	MODIS	14/12/2016 02:35 a.m.	23.59	39.72	
Match-up 2	MWI	16/12/2016 02:34 a.m.	47.11	22.18	91
	MODIS	16/12/2016 04:05 a.m.	24.56	39.73	
Match-up 3	MWI	16/12/2016 14:50 p.m.	45.08	22.12	45
	MODIS	16/12/2016 15:35 p.m.	23.42	39.66	
Match-up 4	MWI	16/12/2016 22:50 p.m.	51.11	22.05	75
	MODIS	16/12/2016 21:35 p.m.	27.13	39.71	
Match-up 5	MWI	20/12/2016 21:55 p.m.	44.06	22.06	45
	MODIS	20/12/2016 21:10 p.m.	26.95	39.74	
Match-up 6	MWI	20/12/2016 23:27 p.m.	39.14	22.02	37
	MODIS	20/12/2016 22:50 p.m.	26.17	39.73	

2.3. Major Differences between MWI and MODIS

Several significant differences exist between MWI and MODIS. First, the quantization level of MWI is 14 bits, which provides four times the radiometric resolution of the 12-bit data from MODIS instruments. Another difference is that the spatial resolution of MWI is 100 m which is nine times higher than that of MODIS 1000 m images. In this paper, the MWI and MODIS images were first projected to geographic coordinates, and the MWI images were then resampled to 1000 m using the mean filtering assuming that each MODIS pixel corresponds to the mean value of the 100 MWI pixels. The third major difference lies in the discrepancy of the relative spectral response (RSR) function between MWI and MODIS. Figure 2 presents the RSRs of TG-2/MWI and Aqua/MODIS. The case 1 water reflectance from United States Geological Survey (USGS) spectral library (<http://speclab.cr.usgs.gov/>) is also plotted in Figure 2, which can be used to calculate the spectral band adjustment factors (SBAFs) for different sensors. The TG-2/MWI has wider bandwidths in the visible and NIR bands than the corresponding bands of the Aqua/MODIS. These discrepancies would eventually affect the spectral sensitivity of the water signatures and signals recorded by various sensors. Therefore, the spectral adjustment between the two different sensors has to be completed [17].

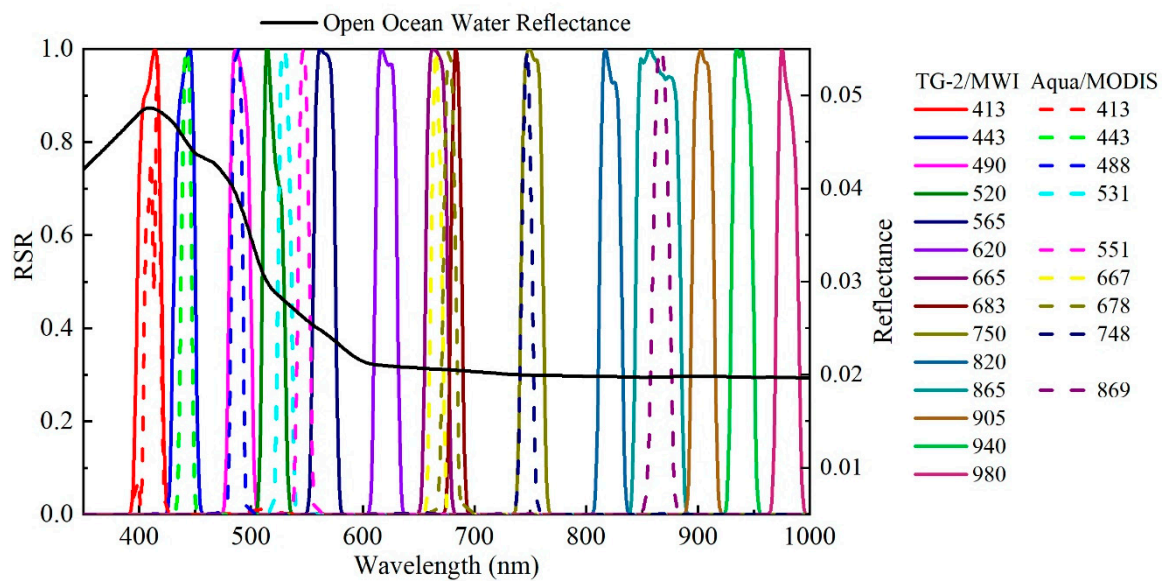


Figure 2. The relative spectral response (RSR) functions of TG-2/MWI (solid lines) and Aqua/MODIS (dashed lines). The black line is open ocean water (case 1 water) reflectance from the United States Geological Survey (USGS) spectral library (<http://speclab.cr.usgs.gov/>).

3. Methodology

The fundamental assumption of this study is that the remote sensing reflectance and the aerosol type remain the same in the same location during the overpassing time of MWI-MODIS match-ups with the adjusted spectral responses and view geometries [12,22]. The basic workflow was first to retrieve the normalized water-leaving reflectance from the TOA signal of MODIS (ρ_{wn}^{MODIS}) through atmospheric correction using NIR-AC algorithm [23]. Then, ρ_{wn}^{MODIS} could be converted into the normalized water-leaving reflectance of the MWI (ρ_{wn}^{MWI}) by applying spectral adjustments. The path radiance of MWI then could be simulated through backward atmospheric radiation transfer modeling, where the view zenith and azimuth angles were from the MWI, with aerosol types determined by MODIS data. Furthermore, the TOA radiance could be calculated. Finally, using a linear regression between the TOA radiances and the digital numbers (DNs) of the MWI images, the calibration coefficients could be obtained. Figure 3 shows the cross-calibration process in this study and major steps are discussed in detail in Sections 3.1–3.3.

3.1. Spectral Adjustment

Before performing the cross-calibration of the TG-2/MWI, the difference between the spectral response of the target sensor and that of the reference sensor was first eliminated using spectral band adjustment factors (SBAF). The formula of SBAF is as follows [17,35]:

$$SBAF = \frac{\int_{a1}^{b1} \rho_{\lambda} \cdot S_{MWI}(\lambda) / \int_{a1}^{b1} S_{MWI}(\lambda)}{\int_{a2}^{b2} \rho_{\lambda} \cdot S_{MODIS}(\lambda) / \int_{a2}^{b2} S_{MODIS}(\lambda)} \quad (1)$$

where $S_{MWI}(\lambda)$ and $S_{MODIS}(\lambda)$ are the relative spectral response functions for the MWI and MODIS, respectively; $a1$ – $b1$ is the spectral range of the MWI; $a2$ – $b2$ is the spectral range of the MODIS; ρ_{λ} is the continuous spectral reflectance of the target. The open ocean seawater reflectance from USGS spectral library was used to calculate SBAFs between the MWI and MODIS. The values of SBAFs are given in Table 3.

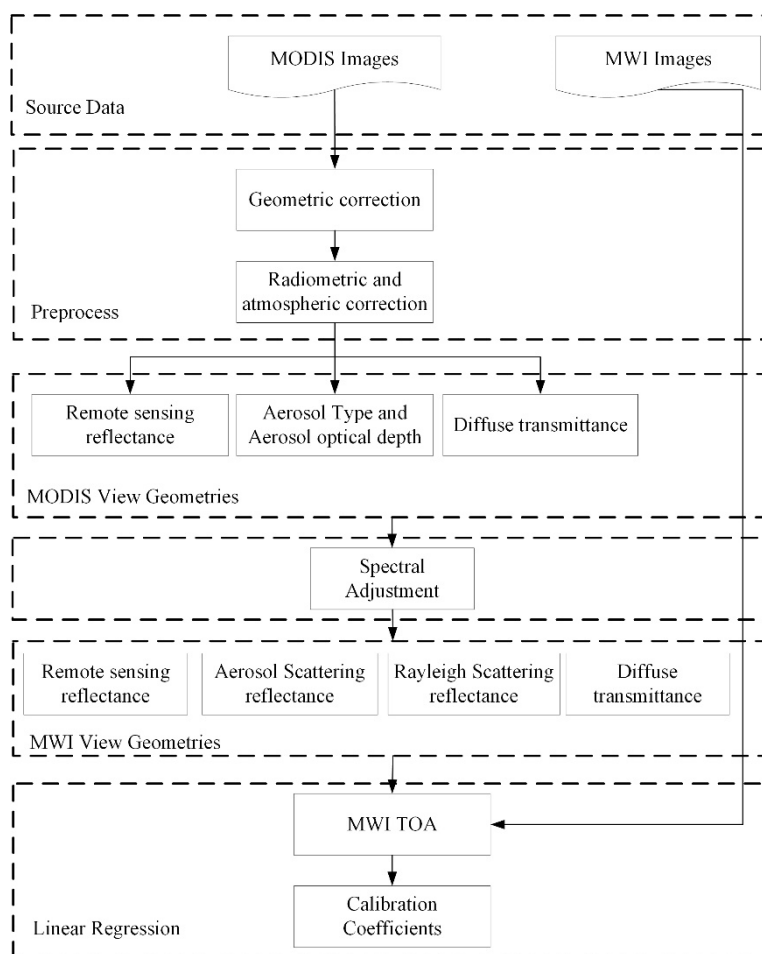


Figure 3. Flowchart of the cross-calibration of MWI using MODIS images. Note: TOA, Top of Atmosphere.

Table 3. Spectral adjustment factors between MWI and MODIS.

Band.	V1	V2	V3	V4	V5	V7	V8	V9	V11
SBAF MWI	1.0103	1.007	0.9772	1.0483	0.9360	1.0002	0.9979	0.9985	0.9999

3.2. TOA Reflectance Calculation

The total signal received by satellite sensors (TOA radiance) responds linearly to the incoming signal. Using the radiance rescaling gains and bias [36], the quantized standard DNs of MWI can be converted to TOA spectral radiance $L_{TOA(MWI,i)}$. Thus, for a given band i of MWI images, the relationship between the TOA radiance and the image DNs can be written as follows:

$$L_{TOA(MWI,i)} = Gain_{MWI,i} \times DN_{MWI,i} + Offset_{MWI,i} \tag{2}$$

where $Gain_{MWI,i}$ is the band-specific multiplicative rescaling gain and $Offset_{MWI,i}$ is the band-specific additive rescaling bias. The radiance can then be converted to TOA reflectance by the following formula:

$$\rho_{TOA(MWI,i)} = \pi \cdot L_{TOA(MWI,i)} \cdot d^2 / (E_{MWI,i} \cdot \cos \theta_{MWI,s}) \tag{3}$$

where $\rho_{TOA(MWI,i)}$ is the TOA reflectance of band i ; $\theta_{MWI,s}$ is the solar zenith angle and d is the distance between the sun and the earth in astronomical units [36], and $E_{MWI,i}$ is the average extra-atmospheric solar spectral irradiance that can be calculated as follows:

$$E_{MWI,i} = \int_a^b f(\lambda) \cdot S_{MWI,i}(\lambda) d\lambda / \int_a^b S_{MWI,i}(\lambda) d\lambda \quad (4)$$

where $f(\lambda)$ is the continuous extra-atmospheric solar spectral irradiance obtained by [37]; $S_{MWI,i}(\lambda)$ is the normalized spectral response function of band i ; a and b are the lower and upper bounds of the spectral range for band i , respectively.

$$\rho_{TOA(MODIS,i)} = Gain_{MODIS,i} \times DN_{MODIS,i} + Offset_{MODIS,i} \quad (5)$$

where $Gain_{MODIS,i}$ is the band-specific multiplicative rescaling factor and $Offset_{MODIS,i}$ is the band-specific rescaling factor obtained from the metadata $DN_{MODIS,i}$, which is the quantized standard pixel value of MODIS product.

3.3. Atmospheric Correction of MWI

In general, for a remote-sensing satellite over water targets, the radiance received by a sensor at the TOA in a spectral band centered at a wavelength λ_i , can be written as Equation (6), supposing the effects of sun glitter [38] and whitecaps [39] are excluded.

$$L_{TOA}(\lambda_i) = L_{path}(\lambda_i) + t(\lambda_i)L_w(\lambda_i) \quad (6)$$

where L_{TOA} stands for radiance measured by the sensor at TOA; L_{path} and L_w are the atmospheric path radiance and water-leaving radiance, respectively; and t is the diffuse transmittance. Similar to Equation (3), $\rho = \pi \cdot L \cdot d^2 / (E \cdot \cos\theta_0)$, the Equation (6) can be normalized to the incident light to yield a dimensionless reflectance term:

$$\rho_{TOA}(\lambda_i) = \rho_{path}(\lambda_i) + t(\lambda_i)\rho_w(\lambda_i) \quad (7)$$

where $\rho_{path} = \rho_r + \rho_a + \rho_{ra}$, ρ_r is the Rayleigh scattering, ρ_a is the aerosol scattering, and ρ_{ra} is the scattering between molecules and aerosols; ρ_r , ρ_a and ρ_{ra} depend on the abundance and type of aerosols [40]. Additionally, ρ_r can be computed accurately from the Rayleigh lookup tables (LUTs) that are prepared using the vector radiative transfer theory with inputs of the solar-sensor geometry, atmospheric pressure and wind speed without considering aerosols [22,41,42].

3.3.1. Rayleigh Scattering of MWI

The Rayleigh scattering at MWI bands was converted from the Rayleigh scattering radiance at MODIS bands, which were calculated using the Rayleigh LUTs. First, the MODIS band-averaged Rayleigh scattering radiance was converted to the band-centered Rayleigh scattering radiance by a conversion factor β , which was calculated by Equation (8):

$$\beta = \tau_r(\lambda_0) / \langle \tau_r(\lambda) \rangle^{MODIS} \quad (8)$$

where $\tau_r(\lambda_0)$ is the Rayleigh optical thickness in the central wavelength λ_0 , and $\langle \tau_r(\lambda) \rangle^{MODIS}$ is the band-averaged Rayleigh optical thickness which is given as follows:

$$\langle \tau_r(\lambda) \rangle^{MODIS} = \int \tau_r(\lambda) S(\lambda) F_0(\lambda) d\lambda / \int S(\lambda) F_0(\lambda) d\lambda \quad (9)$$

where $S(\lambda)$ is the RSR of MODIS bands [43] and $\tau_r(\lambda)$ can be calculated using Equation (10):

$$\tau_r(\lambda) = 0.008569\lambda^{-4}(1 + 0.0113\lambda^{-2} + 0.00013\lambda^{-4}), \lambda \text{ in } \mu\text{m} \quad (10)$$

According to previous study [44], β was estimated as 1.0278, 0.9973, 0.9963, 0.9968, 0.9999, 1.0028, 0.9806, and 0.9904 for MODIS bands at 412, 443, 488, 531, 667, 678, 748, and 869 nm, respectively.

After obtaining the MODIS band-centered Rayleigh scattering reflectance, the dependency in λ^{-4} was used to calculate the sensor-independent ρ_r in the wavelength ranging from 400 to 900 nm [44], because the Rayleigh scattering reflectance ρ_r is $\propto \tau_r \propto \lambda^{-4}$ [45].

Finally, the means of band response-averaged calculation [46] was used to obtain the MWI band-averaged Rayleigh scattering radiance according to Equation (9):

$$\langle L_r(\lambda) \rangle^{MWI} = \int L_r \cdot S(\lambda) d\lambda / \int S(\lambda) d\lambda \quad (11)$$

where L_r is the Rayleigh scattering radiance from the approximated using λ^{-4} function and $\langle L_r(\lambda) \rangle^{MWI}$ is the MWI band-averaged Rayleigh scattering radiance.

3.3.2. Aerosol Scattering of MWI

To calculate the aerosol scattering of MWI images, we first used the NIR-AC algorithm [23] to process the concurrent MODIS scene and generated MODIS aerosol reflectance at 869 nm ($\rho_a^{MODIS}(869)$) and aerosol model for each MODIS pixel. In the open ocean waters, the water leaving signal (ρ_w) in the NIR region (748 nm and 869 nm) is negligible [23]. Thus, the $\rho_a(748)$ and $\rho_a(869)$ are known after subtracting Rayleigh signal from TOA signal (Equation (7)), and were used to derive the atmospheric-correction parameter $\epsilon(\lambda_i, \lambda_j)$ which is defined as follows:

$$\epsilon(\lambda_i, \lambda_j) \equiv \frac{\rho_{as}(\lambda_i)}{\rho_{as}(\lambda_j)} = \frac{w_a(\lambda_i)\tau_a(\lambda_i)P_a(\theta, \theta_0, \lambda_i)}{w_a(\lambda_j)\tau_a(\lambda_j)P_a(\theta, \theta_0, \lambda_j)} \quad (12)$$

where w_a , τ_a , and P_a are, respectively, the aerosol single-scattering albedo, the aerosol optical thickness, and the aerosol scattering phase function. After $\epsilon(748, 869)$ is known, the aerosol models which closely bracket the $\epsilon(748, 869)$, could be selected for each MODIS pixel from the aerosol LUTs.

For each MWI pixel, we identified the corresponding MODIS pixel for the aerosol models. The aerosol scattering of MWI $\rho_a^{MWI}(\lambda)$ was derived as follows [22]:

(1) Convert MODIS aerosol multiple scattering to MODIS aerosol single scattering at MODIS view geometries: $\rho_a^{MODIS}(869)$ at $(\theta_0, \theta, \Delta\varphi)^{MODIS} \Rightarrow \rho_{as}^{MODIS}(869)$ at $(\theta_0, \theta, \Delta\varphi)^{MODIS}$. Three coefficients in aerosol LUTs relate the multiple scattered signal to the single scattered signal using a quadratic relation of the following form:

$$\log(MS) = c \times \log(SS)^2 + b \times \log(SS) + a \quad (13)$$

where MS and SS mean multiple scattering and single scattering, respectively; and a , b , c are parameters in aerosol LUTs. Using the coefficients embedded in LUTs, the multiple scattered signal could be easily converted to a single scattered signal according to Equation (12).

(2) Calculate MWI aerosol single scattering at 869 nm at MWI view geometries according aerosol phase function in LUTs: $\rho_{as}^{MODIS}(869)$ at $(\theta_0, \theta, \Delta\varphi)^{MODIS} \Rightarrow \rho_{as}^{MWI}(869)$ at $(\theta_0, \theta, \Delta\varphi)^{MWI}$. According to Equation (11), $\rho_{as}^{MWI}(869, \theta_0, \theta, \Delta\varphi)^{MWI} = w_a(869)\tau_a(869)P_a(\theta, \theta_0, 869)^{MWI}$ and can be written as follows:

$$\rho_{as}^{MWI}(869, \theta_0, \theta, \Delta\varphi)^{MWI} = \rho_{as}^{MODIS}(869, \theta_0, \theta, \Delta\varphi)^{MODIS} \frac{P_a(\theta, \theta_0, 869)^{MWI}}{P_a(\theta, \theta_0, 869)^{MODIS}} \quad (14)$$

(3) MWI aerosol single scattering in the wavelength ranging from 400 to 900 nm were interpolated from $\rho_{as}^{MWI}(869)$ at MWI view geometries according spectral ρ_{as} relationship from aerosol LUTs: $\rho_{as}^{MWI}(869)$ at $(\theta_0, \theta, \Delta\varphi)^{MWI} \Rightarrow \rho_{as}^{MWI}(\lambda)$ at $(\theta_0, \theta, \Delta\varphi)^{MWI}$ [44].

(4) Convert MWI aerosol single scattering to MWI aerosol multiple scattering according to Equation (13);

$$\rho_{as}^{MWI}(\lambda) \text{ at } (\theta_0, \theta, \Delta\varphi)^{MWI} \Rightarrow \rho_a^{MWI}(\lambda) \text{ at } (\theta_0, \theta, \Delta\varphi)^{MWI}$$

(5) Use the means of band response-averaged calculation to obtain the band-averaged MWI aerosol multiple scattering:

$$\langle \rho_r(\lambda) \rangle^{MWI} = \int \rho_a^{MWI}(\lambda) S(\lambda) F_0(\lambda) d\lambda / \int S(\lambda) F_0(\lambda) d\lambda \quad (15)$$

where $\langle \rho_r(\lambda) \rangle^{MWI}$ is the band response-averaged aerosol scattering of MWI; $\rho_a^{MWI}(\lambda)$ is the aerosol scattering in the wavelength ranging from 400 to 900 nm; and $S(\lambda)$ is the RSR of MWI bands.

3.3.3. Water-Leaving Reflectance of MWI

Previous studies have proven that MODIS images can estimate water-leaving reflectance (ρ_w) with a low level of uncertainty [47–49]. The disparities in ρ_w between the MWI and MODIS data are caused by two factors. One is the spectral differences between of the two sensors which is eliminated by spectral adjustments (Section 3.1). Another is the difference in the atmospheric radiation transfer process caused by view geometries. To reduce the influence of view geometries, remote sensing reflectance was used as a medium to convert ρ_w of MODIS to ρ_w of MWI. Remote sensing reflectance R_{rs} is written as follows:

$$R_{rs} = \frac{\rho_w}{\pi \cdot t_0(\theta_0)} \quad (16)$$

where t_0 is the diffuse transmittance along the sun-to-pixel path, and θ_0 is the solar-zenith angle. The diffuse transmittance of the atmosphere is given approximately by Equation (17) [23]:

$$t_0 = \exp[-(\tau_r/2 + \tau_{OZ})/\cos\theta_0] \quad (17)$$

where τ_r is the Rayleigh optical thickness calculated in Equation (10), and τ_{OZ} is the ozone optical thickness which was derived from ozone file embedded in SeaDAS7.4. For simplicity, the wavelength dependency of the above variables has been suppressed. Thus, the water leaving reflectance of MODIS, ρ_w^{MODIS} , can be converted to that of MWI, ρ_w^{MWI} in the following formula:

$$\frac{\rho_w^{MWI}}{\pi \cdot t_0(\theta_0^{MWI})} = \frac{\rho_w^{MODIS}}{\pi \cdot t_0(\theta_0^{MODIS})} \quad (18)$$

and Equation (18) can be transferred to following form:

$$\rho_w^{MWI} = \frac{\rho_w^{MODIS} \cdot t_0(\theta_0^{MWI})}{t_0(\theta_0^{MODIS})} \quad (19)$$

Finally, linear interpolation was adopted to obtain the ρ_w^{MWI} at MWI bands.

4. Results and Discussion

4.1. Cross-Calibration Results

The radiometric calibration coefficients of the MWI were calculated using the proposed method, based on the selected areas in the open ocean test sites. As the SNRs of MWI are much lower than that of MODIS (Table 1), in this paper, we selected many matched areas (>150) in the six match-ups and used the mean value of each area to present the area (each area should be larger

than a 5×5 window). Taking this approach, the noises and the register errors could be reduced. Doing this was very important because no reference points existed for the geometric registration in open oceans. With sufficient calibration areas, a linear regression between the DNs and the simulated TOA radiance resulted in cross-calibration coefficients (both gains and offsets) for the MWI sensor. Figure 4 plots the simulated TOA radiance against the DNs for the nine spectral bands of MWI. The points for all the spectral bands are aligned along a linear fitting line (with $R^2 > 0.97$), suggesting the statistical significance of the linear fits and the validity of the regression coefficients. The obtained cross-calibration coefficients and lab calibration coefficients of TG-2 MWI are listed in Table 4.

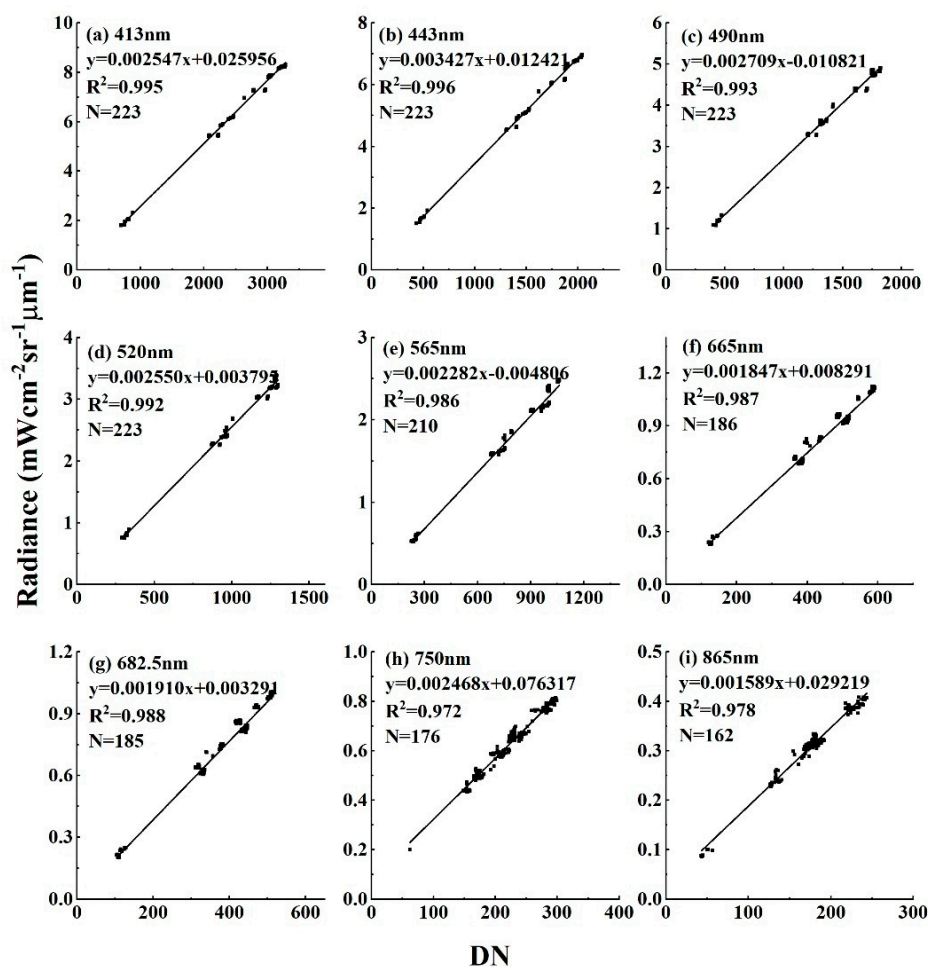


Figure 4. MODIS simulated TOA radiances against the MWI digital numbers (DN) for the nine spectral bands of MWI.

Table 4. Cross-calibration coefficients of the nine bands of TG-2/MWI.

Bands	Center Wavelength (nm)	Cross-Calibration Coefficients		Lab-Calibration Coefficients		R^2	N
		Gains	Offsets	Gains	Offsets		
V1	413	0.002547	0.025956	0.002236	−0.142702	0.995	223
V2	443	0.003427	0.012421	0.003204	−0.210375	0.996	223
V3	490	0.002709	−0.010821	0.002612	−0.158392	0.993	223
V4	520	0.002550	0.003795	0.002438	−0.138600	0.992	223
V5	565	0.002282	−0.004806	0.002149	−0.107429	0.986	210
V7	665	0.001847	0.008291	0.001903	−0.081544	0.987	186
V8	682.5	0.001910	0.003291	0.001991	−0.088102	0.988	185
V9	750	0.002468	0.076317	0.002206	−0.097527	0.972	176
V11	865	0.001589	0.029219	0.001581	−0.054165	0.978	162

4.2. Validation Results

The validation in this study was slightly different from some publications that evaluated the calibration coefficients using in-situ measurements [12]. Unfortunately, synchronized ground-measurement data were not collected. Therefore, we selected the different MWI-MODIS match-ups for validation. The procedure was carried out by the following steps: (1) Choose image pairs of the MWI and MODIS with similar transit times at open ocean waters; the information of these chosen image pairs are listed in Table 5. Note that the match-ups for validation are different with those for cross-calibration; (2) calculate the TOA radiance of these MWI images using the cross-calibration coefficients and lab calibrated coefficients, separately; (3) simulate the TOA radiance using synchronous MODIS images; (4) compare the three sets of TOA radiance. Root mean square error (RMSE), mean bias (MB, %) and mean ratio (MR) were calculated to represent the uncertainties of the cross-calibration coefficients. The comparisons are shown in Figure 5.

Compared to the TOA radiance simulated from synchronized MODIS images, the MBs of the TOA radiance calculated with the cross-calibrated coefficients in this paper were less than 5.2%, which were much lower than that calculated with the lab calibrated coefficients. The MRs between cross-calibrated TOA radiance and simulated TOA radiance were within 1 ± 0.03 , which was closer than that of lab-calibrated coefficients. Consequently, the calibration coefficients retrieved in this paper had much higher accuracy and the cross-calibration method performed excellently for the TG-2/MWI. Overall, the performance of this method was relatively better in the visual bands than the NIR bands.

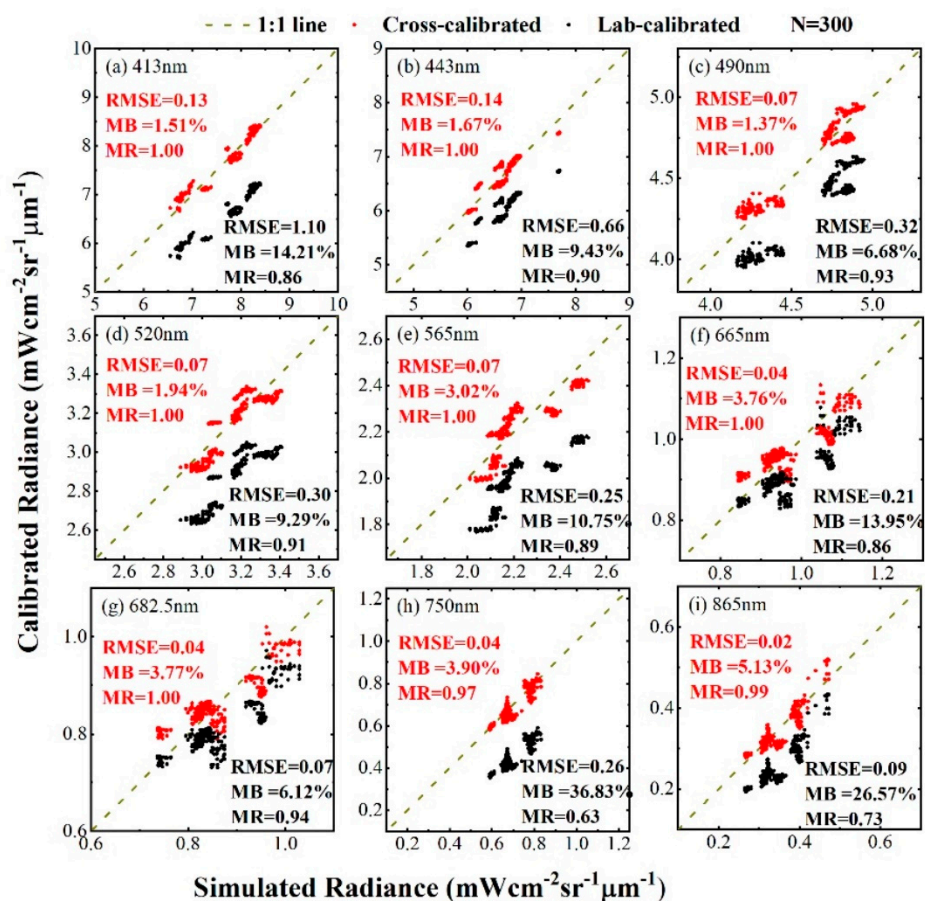


Figure 5. Evaluation of calibrated TOA radiance of MWI using simulated TOA radiance from concurrent MODIS images. RMSE, MB and MR are root mean square errors, mean bias and mean ratio, respectively.

Table 5. Acquisition times, imaging geometries and locations of MWI and MODIS match-ups for validation.

Match-Ups Scenes	Acquisition Time (DD/MM/YYYY HH:MM)	Solar Zenith Angle (°)	Sensor Zenith Angle (°)	Location (°N, °E)	Time Difference (minute)
1 MWI MODIS	13/10/2016 06:45 a.m. 13/10/2016 06:21 a.m.	35.65 36.24	20.80 39.74	(−19.03, 112.77)	24
2 MWI MODIS	04/12/2016 21:10 p.m. 04/12/2016 22:24 p.m.	46.13 28.85	21.01 39.74	(−33.64, −107.76)	74
3 MWI MODIS	14/12/2016 02:35 a.m. 14/12/2016 01:25 a.m.	39.09 23.60	22.05 39.71	(−16.99, 113.76)	70
4 MWI MODIS	14/12/2016 20:07 p.m. 14/12/2016 18:25 p.m.	46.12 34.82	21.81 39.79	(−39.50, −73.93)	102
5 MWI MODIS	15/12/2016 23:10 p.m. 15/12/2016 21:56 p.m.	33.10 27.00	22.22 39.70	(−29.92, 170.59)	74

5. Discussion

This study developed a simple and effective cross-calibration method for TG-2/MWI which was designed for ocean color remote sensing and lacked calibration experiments. The open ocean waters were selected as the calibration sites for its homogenous surface material and low reflectance. Using sufficient areas for calibration can provide a wide range of radiances and DN_s. The well-calibrated MODIS data and MODIS LUTs in SeaDAS 7.4 were used to cross-calibrate MWI. This method does not require accurate geometric registration between the target and reference sensors, because the open ocean waters are temporally, spatially and radiationally stable in brightness and spatial homogeneity. In addition, the cross-calibration method only requires synchronized MODIS images.

In general, it is desirable to consider the bidirectional characteristics of the water surface in the cross-calibration steps, however, it was not considered in our study. We ignored the water surface bidirectional effects for the following reasons: First, the water-leaving signal of open ocean waters accounts for little of total TOA signal. The TOA radiance observed over a clear ocean mainly comes from the atmospheric molecular scattering [50]. Only considering the Rayleigh scattering signal could calibrate satellite sensors with a high accuracy [28,51,52]. Second, the values of bidirectional effects for the sea surface are always smaller for the short-wave segment of the light spectrum (420–550 nm) than for middle and long-wave ones [34]. According to Figure 2, the open ocean water reflectance in middle and long-wave spectrum (>600 nm) is less than 0.02 which is much smaller than that in short-wave spectrum (420–550 nm). Third, bidirectional effects increase rapidly when the zenith angle is >60° [34], however, no solar or view zenith angles of MWI and MODIS collected in our study are larger than 60°.

Given that MWI is an ocean color sensor, we asked whether the cross-calibrated coefficients of MWI could be used to quantify the concentration of water's component? The use of in-situ measurements to evaluate the ocean color products of MWI with the newly derived cross-calibration coefficients is favorable, but it is difficult to collect enough in-situ measurements. Fortunately, the products from synchronous MODIS and GOCI data can be used to evaluate the performance of MWI. The Rayleigh-corrected reflectance (ρ_{rc}), R_{rs} and TSM products of MWI were compared with those products from MODIS and GOCI images for Taihu Lake in China. Taihu Lake (119.5°–120.5°E, 30.5°–31.5°N) was selected as the validation site, which is the third largest freshwater lake and an inland lake in China. The lake has a surface area of 2338 km² with a mean depth of 1.9 m, and has 117 rivers and tributaries draining into the lake [53,54].

5.1. Comparisons of Rayleigh-Corrected Reflectance of MWI, MODIS and GOCI

The solar and sensor viewing angles among MWI, MODIS and GOCI over Taihu Lake are different, and they may influence the Rayleigh-corrected reflectance, however, the spatial distribution and the change tendency should remain consistent. The Rayleigh-corrected reflectance of CMOS/GOCI

(ρ_{rc}^{GOCI}), Terra/MODIS (ρ_{rc}^{MODIS}) and TG-2/MWI (ρ_{rc}^{MWI}) in Taihu Lake on 14 March 2017 are shown in Figure 6. Three bands were selected (the central wavelength is similar). For simplicity, we wrote Band 412 or 413 nm as B_s , Band 660, 667 or 665 nm as B_m , and Band 865 or 869 nm as B_l . Overall, the spatial distributions and dynamic ranges of ρ_{rc} were consistent with each other except B_s of ρ_{rc}^{MWI} and B_m of ρ_{rc}^{MODIS} . For B_m , the dynamic range of ρ_{rc}^{MODIS} (up to ~ 0.08) was lower than that of ρ_{rc}^{MWI} (up to ~ 0.12) and ρ_{rc}^{GOCI} (up to ~ 0.12). The dynamic ranges of ρ_{rc} of CMOS/GOCI and TG-2/MWI in B_m were much higher than that of Terra/MODIS.

The $\rho_{rc}^{MODIS}(B_m)$ is shown in Figure 7 for further analysis. The red frame in Figure 7a and green frame in Figure 7b are two regions of interest (ROI 1 and ROI 2) which appear in the saturated area and the non-saturated area, respectively. In addition, Figure 7c,d shows the mean ρ_{rc} of CMOS/GOCI, TG-2/MWI and Terra/MODIS in the two ROIs, respectively. In Figure 7c, the $\rho_{rc}^{MODIS}(B_m)$ is much less than $\rho_{rc}^{GOCI}(B_m)$ and $\rho_{rc}^{MWI}(B_m)$, and it is also much less than that of the two neighboring bands of Terra/MODIS (551 nm and 678 nm). By comparing Figure 7c with Figure 7d, we can see the ρ_{rc} of CMOS/GOCI, TG-2/MWI and Terra/MODIS is more consistent in the red frame than that in the green frame except B_m . Additionally, the ρ_{rc} in the green frame is smaller than that in the red frame. In summary, the ρ_{rc} of MWI agrees well with both GOCI and Terra for all bands except the ρ_{rc}^{MODIS} (667 nm) in the relative high ρ_{rc} area.

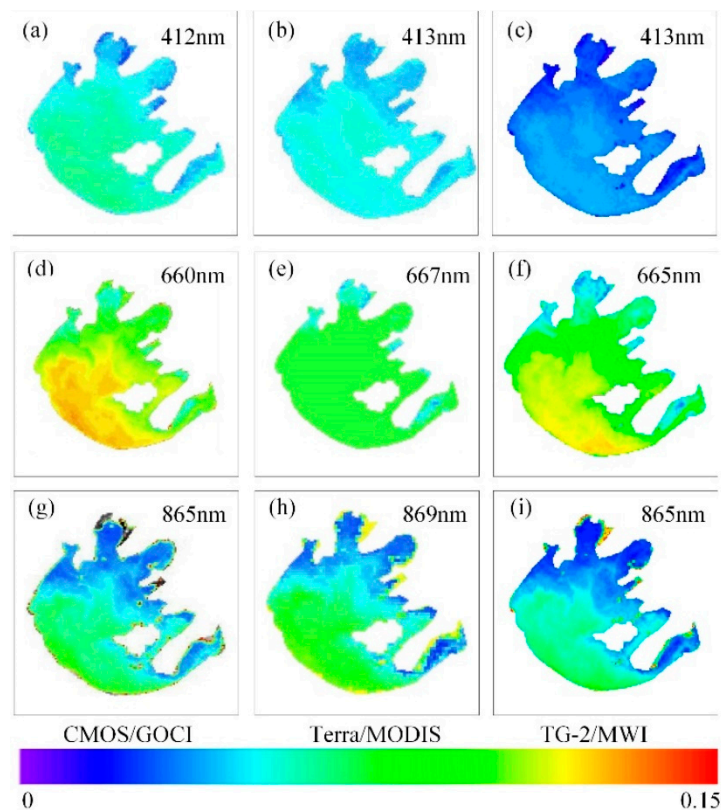


Figure 6. Comparison of the Rayleigh corrected reflectance of Communication, Ocean, and Meteorological Satellite (CMOS)/Geostationary Ocean Color Imager (GOCI) ((a) 412 nm, (d) 660 nm, (g) 865 nm), Terra/MODIS ((b) 413 nm, (e) 667 nm, (h) 869 nm) and TG-2/MWI ((c) 413 nm, (f) 665 nm, (i) 865 nm) of selected bands at 11:16 a.m., 11:00 a.m. and 11:03 a.m. on 14 March 2017, respectively. The time is local time.

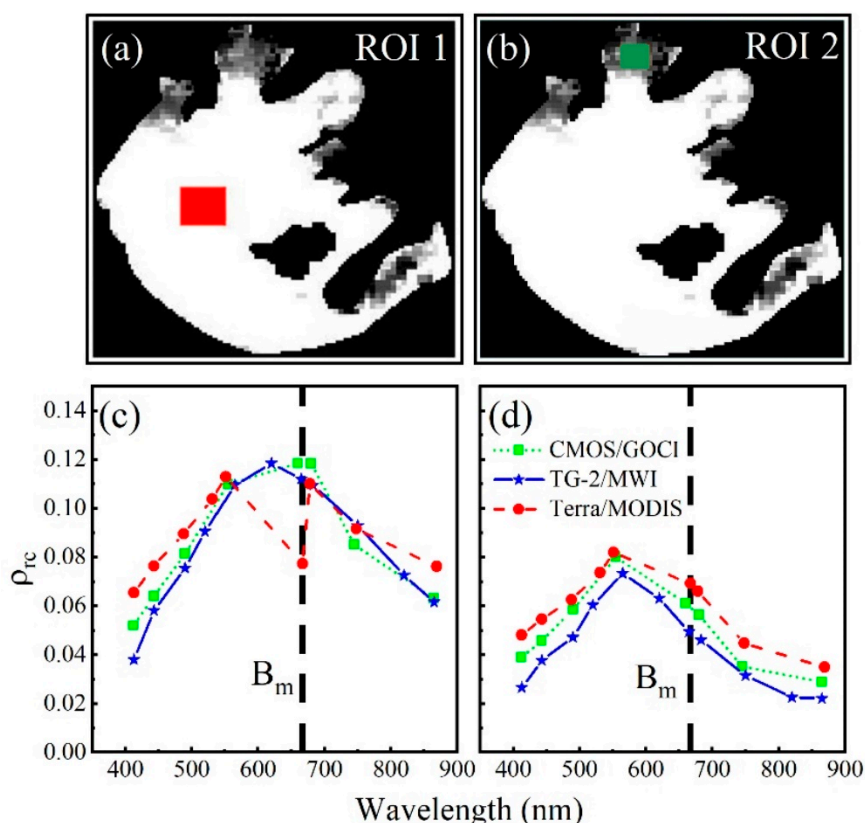


Figure 7. (a) Region of interest (ROI) (red frame) in the saturated part of $\rho_{rc}^{MODIS}(667)$; (b) ROI (green frame) in the normal part of $\rho_{rc}^{MODIS}(667)$; (c) the mean ρ_{rc} of CMOS/GOCI, TG-2/MWI and Terra/MODIS in the red frame; and (d) the mean ρ_{rc} of CMOS/GOCI, TG-2/MWI and Terra/MODIS in the green frame.

5.2. Comparisons of Remote Sensing Reflectance of MWI, MODIS and GOCI

Remote sensing reflectance (R_{rs}) is the fundamental quantity to be derived from ocean color sensors which is the spectral distribution of reflected visible solar radiation upwelling from below the ocean surface and passing through the sea-air interface [23]. Figure 8 shows the MWI- R_{rs} products, GOCI- R_{rs} products and MODIS- R_{rs} products for the TSM retrieval in following section for Taihu Lake, on 14 March 2017. The R_{rs} products were retrieved from turbid Taihu Lake water using ultraviolet atmospheric correction algorithm (UV-AC) [55]. The details of UV-AC are described in Section 5.3. Overall, the spatial distributions of the retrieved R_{rs} were consistent. The R_{rs} values generally increased from the northeast to the southwest part of the lake.

Statistical analyses performed among the TG-2/MWI, Terra/MODIS, and CMOS/GOCI R_{rs} retrievals are shown in Figure 9. The correlation coefficient of TG-2/MWI and Terra/MODIS R_{rs} was 0.93, the MB was 5.52%, the MR was 0.977 and RMSE was 0.020 sr^{-1} . The correlation coefficient, MB, MR, and RMSE between TG-2/MWI and CMOS/GOCI R_{rs} were 0.91, 5.23%, 1.021 and 0.020 sr^{-1} , respectively. Those results indicated that the TG-2/MWI, Terra/MODIS, and CMOS/GOCI R_{rs} agreed well with each other. Overall, the TG-2/MWI was capable of retrieving R_{rs} in inland water. The performance of TG-2/MWI was roughly equivalent to CMOS/GOCI and Terra/MODIS.

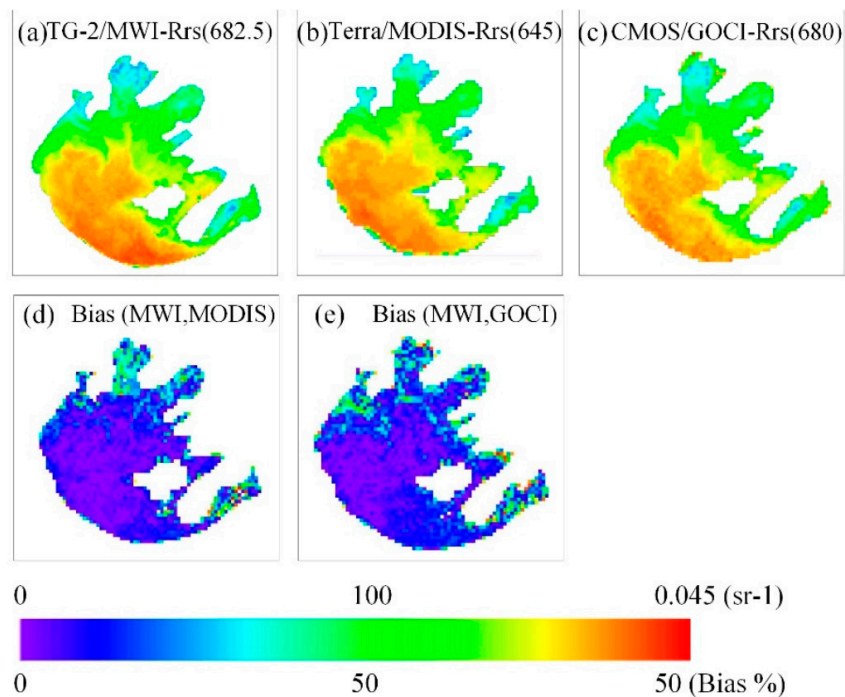


Figure 8. Maps of the remote sensing reflectance (Rrs) products derived from (a) TG-2/MWI, (b) Terra/MODIS and (c) CMOS/GOCI data on 14 March 2017. Biases of Rrs derived from (d) TG-2/MWI and Terra/MODIS (Bias(MWI, MODIS)), and (e) TG-2/MWI and CMOS/GOCI (Bias(MWI, GOCI)) are displayed in the second row.

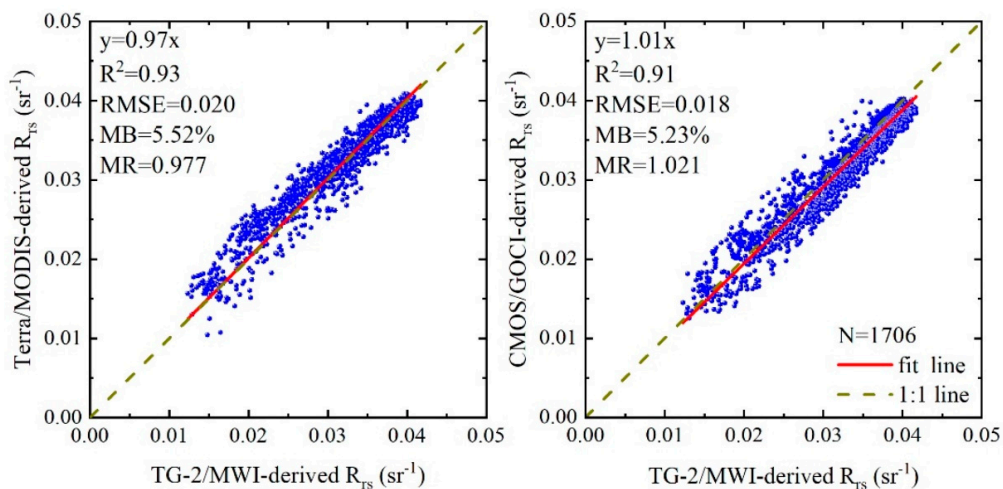


Figure 9. Statistical analysis of TG-2/MWI-derived Rrs, Terra/MODIS-derived Rrs and CMOS/GOCI-derived Rrs products.

5.3. Comparisons of the TSM Retrieved by MWI, MODIS and GOCI

In general, a local TSM algorithm can achieve higher accuracy than the wide-regions applicable algorithms for a specific region. An empirical TSM algorithm [1] developed for Taihu Lake was adopted to retrieve the TSM concentration for TG-2/MWI, CMOS/GOCI and Terra/MODIS imagery in Taihu Lake. The TSM algorithm takes the following form:

$$TSM = \begin{cases} MODIS : 4.812 \times \exp(76.568 \times R_{rs}, 645) \\ GOCI : 6.687 \times \exp(70.870 \times R_{rs}, 680) \\ MWI : 6.154 \times \exp(74.796 \times R_{rs}, 682.5) \end{cases} \quad (20)$$

The atmospheric correction for highly turbid Taihu Lake water was conducted by using the UV-AC [55] and assuming a “white” aerosol scattering reflectance spectrum [56]. The aerosol scattering radiance can be estimated as follows:

$$\begin{cases} \rho_a(865 \text{ nm}) = \rho_{rc}(413 \text{ nm}) \times \exp[c \times (413 - 865)] \\ c = \ln[\rho_{rc}(750 \text{ nm})/\rho_{rc}(865 \text{ nm})]/(865 - 750) \end{cases} \quad (21)$$

As the MODIS band 748 nm was easily saturated in highly turbid waters [57], some relatively “clear” waters in Taihu Lake were selected to determine the aerosol scattering radiance for the whole lake. In addition, SBAFs were adopted to eliminate the difference between the spectral response of different sensors. We used the mean R_{rs} of a single field campaign covering 12 sites conducted in Taihu Lake, on 26 October 2014 to calculate the value of SBAFs. The band coverage of TG-2/MWI and Terra/MODIS to CMOS/GOCI and the in-situ R_{rs} spectra collected in Taihu Lake are shown in Figure 10.

On the basis of the satellite-derived R_{rs} , the TSM concentration was estimated for further analysis. Figure 11 provides a comparison of TSM maps derived from the TG-2/MWI, Terra/MODIS and CMOS/GOCI on 14 March 2017. The biases among the three sensors are also displayed in Figure 11. Clearly, retrieved TSM patterns were spatially well consistent, as shown in Figure 11a–c. Generally, the MWI, MODIS and GOCI TSM products indicated that the spatial variation of TSM concentrations in the Taihu Lake was high. As shown in Figure 11d,e, the biases between TG-2/MWI and Terra/MODIS, as well as between TG-2/MWI and CMOS/GOCI were larger in the near land pixels which might be caused by the adjacency effects [58]. The biases shown in Figure 11d,e were counted and shown in Figure 12. The biases between TG-2/MWI and CMOS/GOCI TSM products (or Terra/MODIS TSM products) of about 80% pixels were less than 20%. This indicated that the TG-2/MWI TSM product agreed well with the CMOS/GOCI TSM product and the Terra/MODIS TSM product.

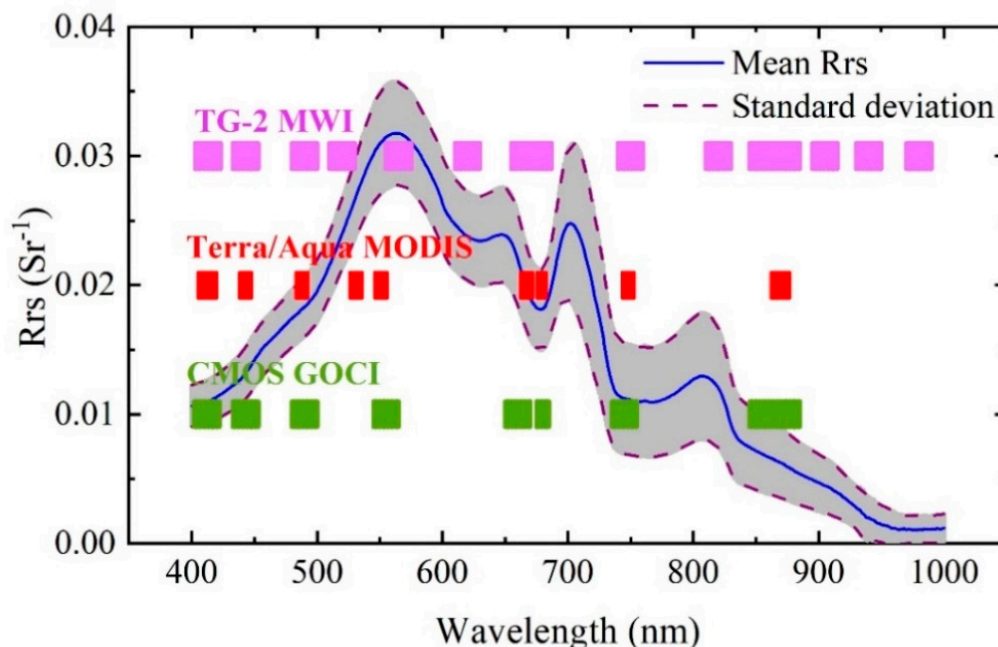


Figure 10. The bands configuration of TG-2 MWI, Terra/Aqua MODIS and CMOS GOCI, overlaid with the mean and standard deviation of R_{rs} at Taihu Lake.

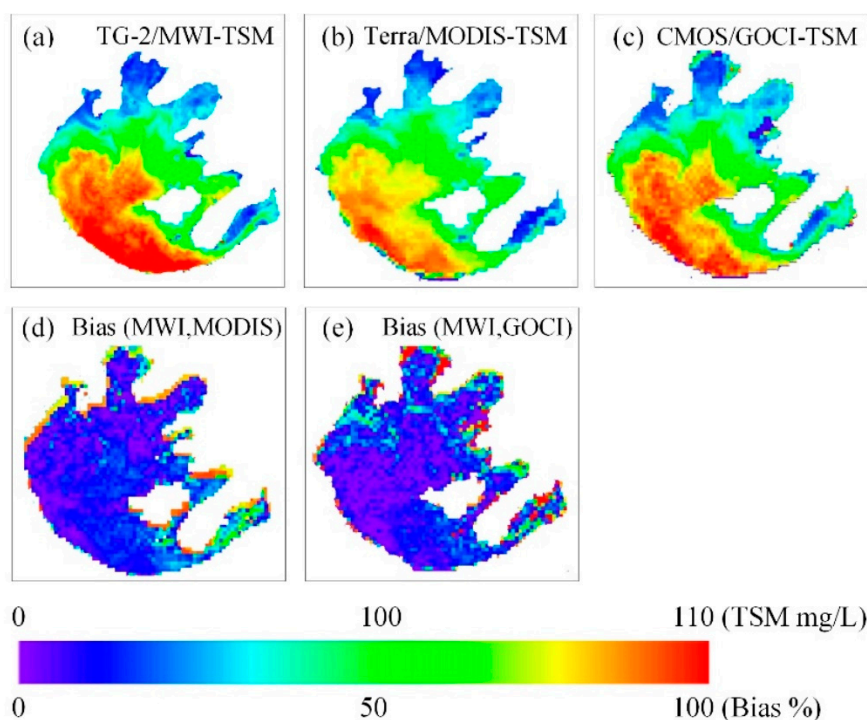


Figure 11. Maps of the total suspended matter (TSM) products derived from (a) TG-2/MWI, (b) Terra/MODIS and (c) CMOS/GOCI data on 14 March 2017. Biases of TSM derived from (d) TG-2/MWI and Terra/MODIS (Bias(MWI, MODIS)), and (e) TG-2/MWI and CMOS/GOCI (Bias(MWI, GOCI)) are displayed in the second row.

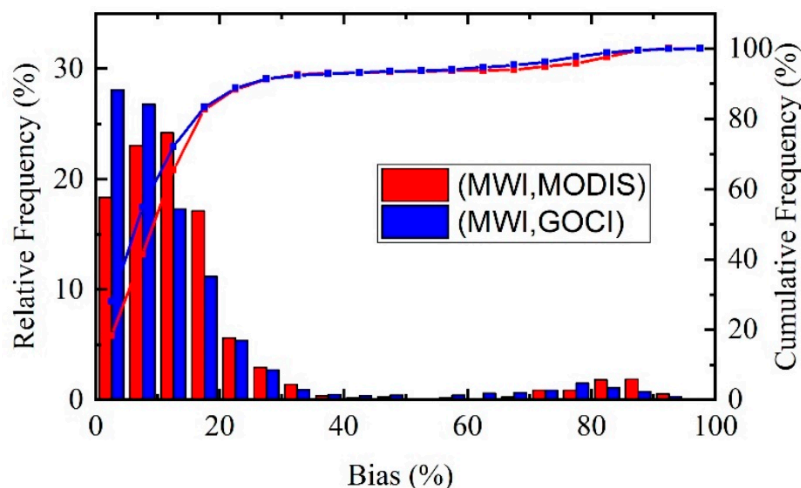


Figure 12. Statistics of frequency distribution of biases between TG-2/MWI-derived TSM and Terra/MODIS-derived TSM, TG-2/MWI-derived TSM and CMOS/GOCI-derived TSM.

Statistical analysis was performed among the TG-2/MWI, Terra/MODIS and CMOS/GOCI TSM products (Figure 13). Note that the pixels near the land were excluded because they might be greatly influenced by adjacent effects and errors of image registration. The correlation coefficient of TG-2/MWI and CMOS/GOCI TSM was 0.90, the MB was 13.75%, the MR was 0.97 and RMSE was 9.43 mg/L (Figure 13b). This showed that the TG-2/MWI and CMOS/GOCI TSM agreed well with each other. However, the agreement was a little worse when the results were compared with Terra/MODIS TSM, with the MR of 0.90 and RMSE of 11.15 mg/L (Figure 13a). Overall, the TG-2/MWI was capable of resolving TSM in inland water. The performance of TG-2/MWI was closer to CMOS/GOCI than Terra/MODIS. The spatial resolution of TG-2/MWI (100 m) is much higher than that of CMOS/GOCI

(500 m), which means that the TG-2/MWI has the potential to perform better in TSM retrieval, such as resolving the fine structures of TSM and monitoring the TSM distribution in small lakes and large rivers.

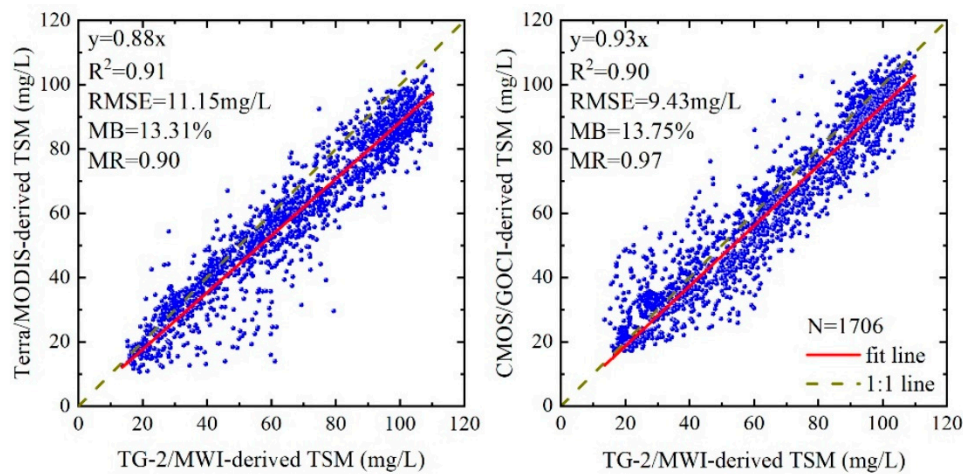


Figure 13. Statistical analysis of TG-2/MWI-derived TSM, Terra/MODIS-derived TSM and CMOS/GOCI-derived TSM products.

6. Conclusions and Future Work

We proposed a simple and effective cross-calibration method for ocean color remote sensing sensors in this paper. In the proposed methods, the multiple Rayleigh scattering and aerosol scattering radiance were calculated from the MODIS LUTs which provided a means to perform AC for TG-2/MWI and similar ocean color remote sensing sensors over aquatic environments. As long as well-calibrated MODIS data are available, the method can be used to monitor and correct the potential reflectance biases caused by sensor degradation in the future. Therefore, the cross-calibration method can be proposed as a routine procedure used to maintain the accuracy and consistency of TG-2/MWI observations.

The validation results indicated that the coefficients obtained by the proposed method were relatively accurate and the application of TSM retrieval demonstrated that the cross-calibration coefficients can be used to derive ocean color remote sensing products, including inland waters. Although the bidirectional reflectance distribution function of the water signal and the overpass time of the two sensors were not discussed thoroughly in this paper (these will be considered in future work), this study will be helpful for the applications of TG-2/MWI for monitoring ocean and inland waters in the future.

The current study also demonstrated the usefulness of MODIS imagery in sensor radiometric calibration for its highly maintained accuracy. The help of the MODIS Rayleigh and aerosol LUTs to calculate the Rayleigh and aerosol contribution to the TOA signal, also, should be acknowledged. The proposed cross-calibration methods provide a way to radiometrically calibrate the TG-2/MWI at a low cost and with a high accuracy. The method may provide a feasible solution to cross calibrate the next generation Chinese ocean color remote sensing sensors.

Author Contributions: Q.Z. and L.T. conceived and designed the experiments; Q.Z. performed the experiments; J.L. and Q.S. helped to outline the manuscript structure; L.T. and J.L. helped Q.Z. and W.L. to prepare the manuscript.

Funding: This research was funded by the National Key R&D Program of China (grants 2018YFB0504900, 2018YFB0504904 and 2016YFC0200900), the National Natural Science Foundation of China (Nos. 41571344, 41701379, 41331174, 41071261, 40906092, 40971193, 41101415, 41401388, 41206169, and 41406205), the China Postdoctoral Science Foundation, the program of Key Laboratory for National Geographic Census and Monitoring, National Administration of Surveying, Mapping and Geoinformation (No. 2014NGCM), Natural Science Foundation of Jiangxi, China (No. 20161BAB213074), Wuhan University LuoJia Talented Young Scholar project,

Dragon 4 proposal ID 32442, entitled “New Earth Observations tools for Water resource and quality monitoring in Yangtze wetlands and lakes (EOWAQYWET)”, LIESMARS Special Research Funding, the High Resolution Earth Observation Systems of National Science and Technology Major Projects (41-Y20A31-9003-15/17), LIESMARS Special Research Funding, the “985 Project” of Wuhan University; Special funds of State Key Laboratory for equipment.

Acknowledgments: We would like to thank Hu Xiuqing for providing and preprocessing Tiangong-2/MWI data and Li Junsheng for providing in-situ Rrs measurements.

Conflicts of Interest: The authors declare no conflict of interest.

References

1. Cao, Z.; Duan, H.; Song, Q.; Shen, M.; Ma, R.; Liu, D. Evaluation of the sensitivity of china’s next-generation ocean satellite sensor mwi onboard the tiangong-2 space lab over inland waters. *Int. J. Appl. Earth Obs. Geoinf.* **2018**, *71*, 109–120. [[CrossRef](#)]
2. He, X.; Bai, Y.; Wei, J.; Ding, J.; Shanmugam, P.; Wang, D.; Song, Q.; Huang, X. Ocean color retrieval from mwi onboard the tiangong-2 space lab: Preliminary results. *Opt. Express* **2017**, *25*, 23955–23973. [[CrossRef](#)] [[PubMed](#)]
3. Jun, W.; Xianqiang, H.; Mingsen, L.; Lei, D. Moderate-resolution ocean color and temperature imager on chinese tian-gong ii space lab. In Proceedings of the 2017 42nd International Conference on Infrared, Millimeter, and Terahertz Waves (IRMMW-THz), Cancun, Mexico, 27 August–1 September 2017; pp. 1–2.
4. McClain, C.R. A decade of satellite ocean color observations. *Annu. Rev. Mar. Sci.* **2009**, *1*, 19–42. [[CrossRef](#)] [[PubMed](#)]
5. He, X.; Pan, D.; Zhu, Q.; Hao, Z.; Gong, F. On-orbit assessment of the polarization response of cocts onboard hy-1b satellite. In Proceedings of the Earth Observing Missions and Sensors: Development, Implementation, and Characterization, Incheon, Korea, 27 October 2010.
6. Goward, S.N.; Chander, G.; Pagnutti, M.; Marx, A.; Ryan, R.; Thomas, N.; Tetrault, R. Complementarity of resourcesat-1 awifs and landsat tm/etm+ sensors. *Remote Sens. Environ.* **2012**, *123*, 41–56. [[CrossRef](#)]
7. Teillet, P.M.; Markham, B.L.; Irish, R.R. Landsat cross-calibration based on near simultaneous imaging of common ground targets. *Remote Sens. Environ.* **2006**, *102*, 264–270. [[CrossRef](#)]
8. Jiang, G.M.; Li, Z.L. Cross-calibration of msg1-seviri infrared channels with terra-modis channels. *Int. J. Remote Sens.* **2009**, *30*, 753–769. [[CrossRef](#)]
9. Gao, C.; Jiang, X.; Li, X.; Li, X. The cross-calibration of cbers-02b/ccd visible-near infrared channels with terra/modis channels. *Int. J. Remote Sens.* **2013**, *34*, 3688–3698. [[CrossRef](#)]
10. Obata, K.; Miura, T.; Yoshioka, H.; Huete, A.; Vargas, M. Spectral cross-calibration of viirs enhanced vegetation index with modis: A case study using year-long global data. *Remote Sens.* **2016**, *8*, 34. [[CrossRef](#)]
11. Gao, H.; Gu, X.; Yu, T.; Liu, L.; Sun, Y.; Xie, Y.; Liu, Q. Validation of the calibration coefficient of the gaofen-1 pms sensor using the landsat 8 oli. *Remote Sens.* **2016**, *8*, 132. [[CrossRef](#)]
12. Feng, L.; Li, J.; Gong, W.; Zhao, X.; Chen, X.; Pang, X. Radiometric cross-calibration of gaofen-1 wfv cameras using landsat-8 oli images: A solution for large view angle associated problems. *Remote Sens. Environ.* **2016**, *174*, 56–68. [[CrossRef](#)]
13. Gao, H.; Gu, X.; Yu, T.; Sun, Y.; Liu, Q. Cross-calibration of gf-1 pms sensor with landsat 8 oli and terra modis. *IEEE Trans. Geosci. Remote Sens.* **2016**, *54*, 4847–4854. [[CrossRef](#)]
14. Chen, Y.; Sun, K.; Li, D.; Bai, T.; Huang, C. Radiometric cross-calibration of gf-4 pms sensor based on assimilation of landsat-8 oli images. *Remote Sens.* **2017**, *9*, 811. [[CrossRef](#)]
15. Chander, G.; Meyer, D.J.; Helder, D.L. Cross calibration of the landsat-7 etm+ and eo-1 ali sensor. *IEEE Trans. Geosci. Remote Sens.* **2004**, *42*, 2821–2831. [[CrossRef](#)]
16. Teillet, P.M.; Fedosejevs, G.; Thome, K.J.; Barker, J.L. Impacts of spectral band difference effects on radiometric cross-calibration between satellite sensors in the solar-reflective spectral domain. *Remote Sens. Environ.* **2007**, *110*, 393–409. [[CrossRef](#)]
17. Yang, A.; Zhong, B.; Lv, W.; Wu, S.; Liu, Q. Cross-calibration of gf-1/wfv over a desert site using landsat-8/oli imagery and zy-3/tlc data. *Remote Sens.* **2015**, *7*, 10763–10787. [[CrossRef](#)]

18. Sharma, S.; Sridhar, V.N.; Prajapati, R.P.; Rao, K.M.; Mathur, A.K. Absolute Vicarious Calibration of Landsat-8 Oli and Resourcesat-2 Awifs Sensors over Rann of Kutch Site in Gujarat. In *Earth Observing Missions and Sensors: Development, Implementation, and Characterization IV*; International Society for Optics and Photonics: San Diego, CA, USA, 2016; p. 98811J.
19. Xu, W.; Gong, J.; Wang, M. Development, application, and prospects for chinese land observation satellites. *Geo-Spat. Inf. Sci.* **2014**, *17*, 102–109. [[CrossRef](#)]
20. Li, J.; Feng, L.; Pang, X.; Gong, W.; Zhao, X. Radiometric cross calibration of gaofen-1 wfv cameras using landsat-8 oli images: A simple image-based method. *Remote Sens.* **2016**, *8*, 411. [[CrossRef](#)]
21. Vermote, E.F.; Tanre, D.; Deuze, J.L.; Herman, M.; Morcette, J.J. Second simulation of the satellite signal in the solar spectrum, 6s: An overview. *IEEE Trans. Geosci. Remote Sens.* **2002**, *35*, 675–686. [[CrossRef](#)]
22. Hu, C.; Muller-Karger, F.E.; Andrefouet, S.; Carder, K.L. Atmospheric correction and cross-calibration of landsat-7/etm+ imagery over aquatic environments: A multiplatform approach using seawifs/modis. *Remote Sens. Environ.* **2001**, *78*, 99–107. [[CrossRef](#)]
23. Gordon, H.R.; Wang, M. Retrieval of water-leaving radiance and aerosol optical thickness over the oceans with seawifs: A preliminary algorithm. *Appl. Opt.* **1994**, *33*, 443–452. [[CrossRef](#)] [[PubMed](#)]
24. Morel, A.; Prieur, L. Analysis of variations in ocean color. *Limnol. Oceanogr.* **1977**, *22*, 709–722. [[CrossRef](#)]
25. Siegel, D.A.; Wang, M.; Maritorena, S.; Robinson, W. Atmospheric correction of satellite ocean color imagery: The black pixel assumption. *Appl. Opt.* **2000**, *39*, 3582–3591. [[CrossRef](#)] [[PubMed](#)]
26. Wang, M. Remote sensing of the ocean contributions from ultraviolet to near-infrared using the shortwave infrared bands: Simulations. *Appl. Opt.* **2007**, *46*, 1535–1547. [[CrossRef](#)] [[PubMed](#)]
27. Wang, M.; Shi, W. The nir-swir combined atmospheric correction approach for modis ocean color data processing. *Opt. Express* **2007**, *15*, 15722–15733. [[CrossRef](#)] [[PubMed](#)]
28. Chen, X.; Xing, J.; Liu, L.; Li, Z.; Mei, X.; Fu, Q.; Xie, Y.; Ge, B.; Li, K.; Xu, H. In-flight calibration of gf-1/wfv visible channels using rayleigh scattering. *Remote Sens.* **2017**, *9*, 513. [[CrossRef](#)]
29. He, X.; Pan, D.; Zhu, Q.; Gong, F. General exact rayleigh scattering look-up-table for ocean color remote sensing. *Acta Oceanol. Sin.* **2005**, *25*, 145–151.
30. Cosnefroy, H.; Leroy, M.; Briottet, X. Selection and characterization of saharan and arabian desert sites for the calibration of optical satellite sensors. *Remote Sens. Environ.* **1996**, *58*, 101–114. [[CrossRef](#)]
31. Kaufman, Y.J.; Sendra, C. Algorithm for automatic atmospheric corrections to visible and near-ir satellite imagery. *Int. J. Remote Sens.* **1988**, *9*, 1357–1381. [[CrossRef](#)]
32. Angal, A.; Mishra, N.; Xiong, X.; Helder, D. Cross-Calibration of Landsat 5 tm and Landsat 8 Oli with Aqua Modis Using Pics. In *Earth Observing Systems XIX*; International Society for Optics and Photonics: San Diego, CA, USA, 2014; p. 92180K.
33. Pan, D.; He, X.; Zhu, Q. On orbit cross-calibration of cocts onboard hy-1a satellite. *Sci. Bull.* **2004**, *49*, 2239–2244. [[CrossRef](#)]
34. Otremba, Z.; Piskozub, J. Modelling the bidirectional reflectance distribution function (brdf) of seawater polluted by an oil film. *Opt. Express* **2004**, *12*, 1671. [[CrossRef](#)] [[PubMed](#)]
35. Zhong, B.; Zhang, Y.; Du, T.; Yang, A.; Lv, W.; Liu, Q. Cross-calibration of hj-1/ccd over a desert site using landsat etm+ imagery and aster gdem product. *IEEE Trans. Geosci. Remote Sens.* **2014**, *52*, 7247–7263. [[CrossRef](#)]
36. Chander, G.; Markham, B.L.; Helder, D.L. Summary of current radiometric calibration coefficients for landsat mss, tm, etm+, and eo-1 ali sensors. *Remote Sens. Environ.* **2009**, *113*, 893–903. [[CrossRef](#)]
37. Thuillier, G.; Hersé, M.; Labs, D.; Foujols, T.; Peetermans, W.; Gillotay, D.; Simon, P.C.; Mandel, H. The solar spectral irradiance from 200 to 2400 nm as measured by the solspec spectrometer from the atlas and eureka missions. *Sol. Phys.* **2003**, *214*, 1–22. [[CrossRef](#)]
38. Wang, M.; Bailey, S.W. Correction of sun glint contamination on the seawifs ocean and atmosphere products. *Appl. Opt.* **2001**, *40*, 4790–4798. [[CrossRef](#)] [[PubMed](#)]
39. Gordon, H.R.; Wang, M. Influence of oceanic whitecaps on atmospheric correction of ocean-color sensors. *Appl. Opt.* **1994**, *33*, 7754–7763. [[CrossRef](#)] [[PubMed](#)]
40. Antoine, D.; Morel, A. A multiple scattering algorithm for atmospheric correction of remotely sensed ocean colour (meris instrument): Principle and implementation for atmospheres carrying various aerosols including absorbing ones. *Int. J. Remote Sens.* **1999**, *20*, 1875–1916. [[CrossRef](#)]

41. Gordon, H.R.; Brown, J.W.; Evans, R.H. Exact rayleigh scattering calculations for use with the nimbus-7 coastal zone color scanner. *Appl. Opt.* **1988**, *27*, 862–871. [[CrossRef](#)] [[PubMed](#)]
42. Wang, M. A refinement for the rayleigh radiance computation with variation of the atmospheric pressure. *Int. J. Remote Sens.* **2005**, *26*, 5651–5663. [[CrossRef](#)]
43. Eplee, R.E.; Robinson, W.D.; Bailey, S.W.; Clark, D.K.; Werdell, P.J.; Wang, M.; Barnes, R.A.; McClain, C.R. Calibration of seawifs. Ii. Vicarious techniques. *Appl. Opt.* **2001**, *40*, 6701. [[CrossRef](#)] [[PubMed](#)]
44. Zhang, M.; Tang, J.; Dong, Q.; Duan, H.; Shen, Q. Atmospheric correction of hj-1 ccd imagery over turbid lake waters. *Opt. Express* **2014**, *22*, 7906–7924. [[CrossRef](#)] [[PubMed](#)]
45. Gordon, H.R.; Castaño, D.J. Aerosol analysis with the coastal zone color scanner: A simple method for including multiple scattering effects. *Appl. Opt.* **1989**, *28*, 1320–1326. [[CrossRef](#)] [[PubMed](#)]
46. Gordon, H.R. Remote sensing of ocean color: A methodology for dealing with broad spectral bands and significant out-of-band response. *Appl. Opt.* **1995**, *34*, 8363–8374. [[CrossRef](#)] [[PubMed](#)]
47. Vermote, E.F.; Saleous, N.Z.E.; Justice, C.O. Atmospheric correction of modis data in the visible to middle infrared: First results. *Remote Sens. Environ.* **2002**, *83*, 97–111. [[CrossRef](#)]
48. Zhang, H.; Liu, L.; Chen, J. The atmospheric correction of modis imagery for turbid coastal waters. In *Geoinformatics 2006: Remotely Sensed Data and Information*; International Society for Optics and Photonics: San Diego, CA, USA, 2006.
49. Mcatee, B.; Maier, S. *Improved Near-Real Time Atmospheric Correction of Modis Data for Earth Observation Applications*; Springer: Berlin/Heidelberg, Germany, 2009; pp. 149–160.
50. Meygret, A.; Briottet, X.; Henry, P.J.; Hagolle, O. Calibration of spot4 hrvir and vegetation cameras over rayleigh scattering. *Proc. SPIE Int. Soc. Opt. Eng.* **2000**, *4135*, 302–313.
51. Hagolle, O.; Goloub, P.; Deschamps, P.Y.; Cosnefroy, H.; Briottet, X.; Bailleul, T.; Nicolas, J.M.; Parol, F.; Lafrance, B.; Herman, M. Results of polder in-flight calibration. *IEEE Trans. Geosci. Remote Sens.* **1999**, *37*, 1550–1566. [[CrossRef](#)]
52. Briottet, X.; Dilligeard, E.; Santer, R.P.; Deuze, J.L. Vegetation calibration of blue and red channels using rayleigh scattering over open oceans. *Proc. SPIE Int. Soc. Opt. Eng.* **1997**, *3221*, 318–325.
53. Xu, H.; Paerl, H.W.; Qin, B.; Zhu, G.; Gao, G. Nitrogen and phosphorus inputs control phytoplankton growth in eutrophic lake taihu, china. *Limnol. Oceanogr.* **2010**, *55*, 420–432. [[CrossRef](#)]
54. Zhang, Y.; Liu, X.; Yin, Y.; Wang, M.; Qin, B. A simple optical model to estimate diffuse attenuation coefficient of photosynthetically active radiation in an extremely turbid lake from surface reflectance. *Opt. Express* **2012**, *20*, 20482–20493. [[CrossRef](#)] [[PubMed](#)]
55. He, X.; Bai, Y.; Pan, D.; Tang, J.; Wang, D. Atmospheric correction of satellite ocean color imagery using the ultraviolet wavelength for highly turbid waters. *Opt. Express* **2012**, *20*, 20754–20770. [[CrossRef](#)] [[PubMed](#)]
56. Evans, R.H.; Gordon, H.R. Coastal zone color scanner “system calibration”: A retrospective examination. *J. Geophys. Res. Oceans* **1994**, *99*, 7293–7307. [[CrossRef](#)]
57. Zhang, M.W.; Tang, J.W.; Dong, Q.; Song, Q.T.; Ding, J. Retrieval of total suspended matter concentration in the yellow and east china seas from modis imagery. *Remote Sens. Environ.* **2010**, *114*, 392–403. [[CrossRef](#)]
58. Kiselev, V.; Bulgarelli, B.; Heege, T. Sensor independent adjacency correction algorithm for coastal and inland water systems. *Remote Sens. Environ.* **2015**, *157*, 85–95. [[CrossRef](#)]

